

Engraving High-Density Nanogaps in Gold Thin Films via Sequential Anodization and Reduction for Surface-Enhanced Raman Spectroscopy Applications

Kwang Min Baek,^{†,⊥} Jaehoon Kim,^{†,⊥} Shinho Kim,[§] Seunghee H. Cho,[†] Min Seok Jang,[§] Jihun Oh,^{*,†,‡} and Yeon Sik Jung^{*,†}

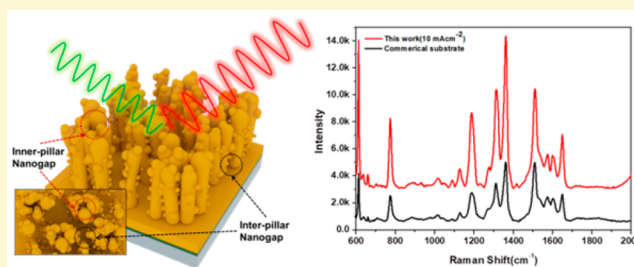
[†]Department of Materials Science and Engineering, Korea Advanced Institute of Science and Technology (KAIST), 291 Daehak-ro, Yuseong-gu, Daejeon 34141, Republic of Korea

[‡]Graduate School of Energy, Environment, Water and Sustainability (EEWS), Korea Advanced Institute of Science and Technology (KAIST), 291 Daehak-ro, Yuseong-gu, Daejeon 34141, Republic of Korea

[§]School of Electrical Engineering, Korea Advanced Institute of Science and Technology (KAIST), 291 Daehak-ro, Yuseong-gu, Daejeon 34141, Republic of Korea

Supporting Information

ABSTRACT: To realize a more rapid and accurate detection technique for diverse trace molecules, surface-enhanced Raman scattering (SERS) analysis has been extensively investigated in recent decades. However, a practical fabrication method to scalably and reproducibly produce SERS substrates with highly effective SERS-active sites and extensive optical tunability still remains an important research target. Here, we present an electrochemical pathway to generate a high-performance SERS substrate. This method provides not only ultrahigh-density hot spots as a form of nanogaps for strong and uniform SERS signal enhancement but also tunable plasmonic properties for capability of matching the plasmonic resonance wavelength with that of the Raman excitation laser. The unique Au nanopillar array decorated with ultrafine Au nanoparticles records a high SERS signal enhancement effect, which enables trace-molecule detection on the entire measured area with highly reproducible signal intensity. Also, via aptamer-functionalization on this substrate, an extremely sensitive and highly selective SERS-based Hg²⁺ ions detection sensor is demonstrated. Trace-amount (10 ppb) Hg²⁺ ions can be selectively identified in a mixture solution containing six different metallic ion species as well as in a beverage containing numerous other components.



INTRODUCTION

With drastically increasing demand for rapid detection of trace target molecules, development of practical analysis tools that have both high signal enhancement and selectivity is essential.¹ Among the alternative detection techniques, surface-enhanced Raman scattering (SERS) spectroscopy is regarded as one of the most attractive detection techniques due to its advantages such as high sensitivity, high selectivity, and simplicity of measurement.^{2–6} SERS analysis is based on the local electric field (E-field) enhancement by plasmonic nanostructures to amplify Raman signals by several orders of magnitude.^{5,7–13} Previous studies have reported various types of plasmonic nanostructures containing high density “hot spots” for local E-field enhancement, which can even realize single-molecule detection.^{14–29} Because the degree of E-field enhancement can be significantly increased as the nanogap size is decreased, the development of practical fabrication techniques for nanogap structures has been widely attempted.^{27,30–40} However, manufacturing plasmonic nanostructures containing extremely narrow nanogaps with sufficient reproducibility remains

challenging. Meanwhile, recent studies reported that the SERS signal intensity is closely correlated with the degree of correspondence between the plasmonic resonance peak and the wavelength of the excitation laser.^{41,42} These results suggest that extremely high Raman signal enhancement can be achieved by the formation of high-density, well-defined nanogap structures with precisely tuned plasmonic resonances.

Well-dispersed metal nanoparticles synthesized on the basis of wet chemical preparation have been widely used to obtain high enhancement of SERS activity, varying the size of nanogaps as well as their shapes.^{32,43–46} In addition, highly ordered metal nanostructures fabricated by template-based electrodeposition have been utilized as an effective SERS-active substrate, exhibiting remarkable and reproducible signal amplification.^{47–49} Although these methods are useful to enhance the SERS signal intensity, the synthesis process is

Received: July 15, 2018

Revised: August 5, 2018

Published: August 6, 2018

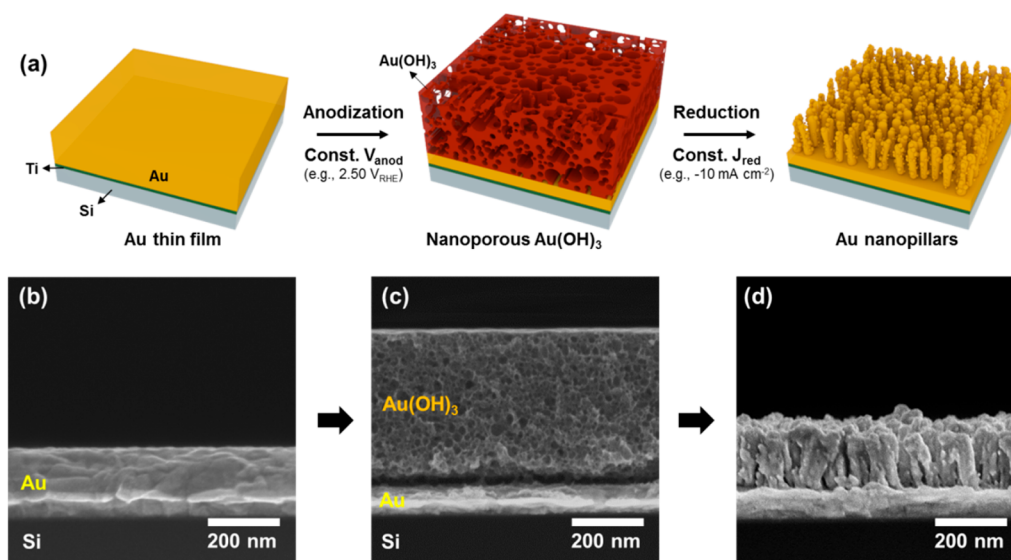


Figure 1. Morphological evolution of Au thin films during reduced anodic (RA) treatment. (a) Schematic illustration of the formation of Au nanopillar arrays via RA treatment. (b–d) Cross-sectional scanning electron microscopy (SEM) images of Au thin film samples before and after RA treatment. (b) Au thin film deposited on the Si substrate with Ti as an adhesion layer. (c) Sponge-like nanoporous Au(OH)₃ layer obtained by potentiostatic anodization of the prepared Au thin film in a 0.2 M KHCO₃ solution. (d) Array of Au nanopillars obtained after subsequent reduction treatment with a relatively high reduction current density (e.g., -10.0 mA cm^{-2}).

time-consuming. Moreover, the presence of process-related impurities, such as capping agents or residues from unremoved templates, may prevent the direct adsorption of target molecules on the hot spots, resulting in reduction of the SERS signal enhancement.⁵⁰ Therefore, developing an alternative strategy to form scalable and well-controlled plasmonic nanostructures via not only a facile pathway but also an additive- or template-free condition is an important task for further improving the SERS activity.

Recently, electrochemical treatments on noble metals have garnered increasing attention as an effective method to fabricate nanostructures.^{51–54} This procedure simply consists of two stages where electrochemical oxidation of metals is first conducted and followed by reduction of oxide forms of metals. Importantly, the shapes of nanostructures can be tuned with control of only electrochemical process parameters without relying on templates and additives.^{54–57} Considering this, the resultant nanostructures prepared by electrochemical treatment can be expected to exhibit highly effective SERS enhancement.

Here, we successfully developed fabrication routes that satisfy multiple goals of simplicity, excellent reproducibility, and high signal enhancement by generating ultrahigh-density nanogaps in gold thin films via an electrochemical process and by matching the plasmonic resonance peak with the excitation laser wavelength. By adapting electrochemically reduced anodic (RA) treatment on flat gold films, nanoporous gold structures composed of ultrahigh density nanogaps were successfully engraved in Au thin films. Also, by controlling the reduction current on oxidized gold films, the resultant unique gold morphology—three-dimensional (3D) structure composed of nanoparticles on nanopillars (NPOP) exhibits tunable plasmonic properties, which further increase the SERS activity at a measured laser wavelength. As a result, a markedly high area-averaged enhancement factor of 10^5 on entire measured area is achieved. Moreover, we show that the nanogap-engraved SERS substrate combined with aptamer

functionalization also acted as a Hg²⁺ ion detection sensor with excellent detection selectivity and sensitivity, and can quantitatively evaluate the concentration of Hg²⁺ ions in complex mixtures.

EXPERIMENTAL SECTION

Fabrication of Au Nanopillar Arrays. A 200 nm-thick Au thin film was e-beam evaporated onto a *p*-type (100) Si wafer (B-doped, resistivity: 5–10 $\Omega\text{-cm}$) with 5 nm-thick Ti as an adhesion layer. The Au electrode (i.e., Au/Ti/Si wafer) was cut into pieces of about 1.5 cm \times 1.5 cm. To remove organic contaminants from the Au surface, each piece was degreased sequentially by acetone and isopropyl alcohol (IPA) followed by deionized (DI) water. Cu wire was then fixed on an edge of the Au film to form an electrical pathway with Ag paste. All edges of the Au film were then covered with a chemically inert and electrical insulating tape (NITOFLON No.903UL, Nitto Denko Co.). The electrochemical treatment, viz. reduced anodic (RA) treatment, was conducted in a typical three-electrode system using an SP-150 potentiostat (Bio-Logic, USA). An Ag/AgCl (in 3 M NaCl) and a Pt coil were used as a reference and a counter electrode, respectively. At the first step for the RA treatment, potentiostatic polarization was performed to anodize the prepared Au electrode by applying 2.5 V (vs reversible hydrogen electrode (RHE)) for 40 min in a 0.2 M KHCO₃ solution (pH 8.4, 99.7% purity of KHCO₃, Sigma-Aldrich) with stirring of 80 rpm at room temperature. Note that all potentials in this work are defined as the RHE by $E_{\text{RHE}} = E_{\text{WE}} + (0.209 + 0.059 \times \text{pH}) \text{ V}$. The surface of the as-anodized Au electrode was briefly rinsed with DI water, and afterward galvanostatic electrochemical reduction, as the second step, was carried out in the same solution with 80 rpm stirring with various reduction current densities until a dramatic potential transition and hydrogen evolution were simultaneously observed. The morphology of the Au nanostructures formed from RA treatment was characterized using a field emission scanning electron microscope (Magellan400, FEI Co.).

Raman Spectroscopy. A high-resolution dispersive Raman spectroscope (ARAMIS, Horiba) with a 514 and 633 nm excitation laser was used for SERS measurements. The SERS signal was collected for 7 s for each measurement. Rhodamine 6G (R6G) was purchased from Sigma-Aldrich, Inc. and used as probe molecules for a performance test after dissolving in ethanol with a concentration of 10^{-6} to 10^{-10} M. We followed the detection procedure of Hg²⁺ and

other metal ions published in a previous study.⁵⁸ Briefly, the SERS/apptamer sensor was immersed for 60 min in a phosphate-buffered saline (PBS) solution containing Hg^{2+} and other metal ions before SERS measurement. For the selectivity test, various ion sources such as CaCl_2 , $\text{Co}(\text{NO}_3)_2$, K_2SO_4 , $\text{Zn}(\text{NO}_3)_2$, and HgCl_2 were used.

Electromagnetic Simulations. The reflection spectra of the pillar array structures were calculated by full-wave electromagnetic simulations using the finite element method (COMSOL Multiphysics). The frequency-dependent dielectric functions of Au and Si were taken from Johnson and Christ⁵⁹ and Palik,⁶⁰ respectively.

RESULTS AND DISCUSSION

A simple and facile yet highly reproducible two-step electrochemical process called reduced anodic (RA) treatment was used to fabricate 3D Au nanostructures, as illustrated in Figure 1a. The formation mechanism of the 3D Au nanostructures as well as the detailed fabrication procedure was reported in our previous study.⁵⁴ Briefly, in the first step, anodization on a thin Au electrode with ca. 200 nm thick was performed by potentiostatic polarization at 2.50 V (vs reversible hydrogen potential (RHE)), all given potential is hereafter expressed as RHE) for 40 min in a 0.2 M KHCO_3 solution. As a result of the anodization, a nanoporous Au hydroxide (i.e., $\text{Au}(\text{OH})_3$) layer was formed on the remaining Au film.^{61,62} Subsequently, as the second step, galvanostatic electrochemical reduction of the $\text{Au}(\text{OH})_3$ was conducted by a relatively high reduction current density, leading to the formation of Au nanopillar arrays. Figure 1b–d shows cross-sectional scanning electron microscopy (SEM) images corresponding to the representative states during RA treatment, as illustrated in Figure 1a. As can be seen, nanoporous $\text{Au}(\text{OH})_3$ with a thickness of about 420 nm was produced from the anodization of the prepared 200 nm-thick Au thin film on a Si substrate (Figure 1b,c). After the electrochemical reduction of the $\text{Au}(\text{OH})_3$ by constantly driving -10 mA cm^{-2} , Au nanopillar arrays vertically standing on the remaining Au thin film with $\sim 200 \text{ nm}$ height were obtained (Figure 1d).

It is well-known that a sub-10 nm nanogap between metal nanostructures generates a localized yet highly intensive electromagnetic field (E-field), resulting in a dramatic increase of the SERS activity.^{32,47,63} Meanwhile, the structural characteristics of Au nanostructures formed via RA treatment can be tuned by control of process parameters, such as anodic potential, time, and reduction current density.^{53,55,64} In particular, by controlling the reduction process parameter, it was seen that not only shapes but also the gaps between nanostructures were varied. This is basically associated with the electric-field-assisted transport of Au^{3+} to the reduction sites. When relatively higher reduction current density was applied, for example, the Au^{3+} ions were preferentially reduced at the tip of the forming Au nanostructures because a high electric-field could be developed around the high-curvature surface (i.e., the tip).^{65,66} This mainly leads to longitudinal growth and thus results in the formation of Au nanopillars. In addition, due to the fast reduction kinetics during the electroreduction, local deficiency of Au^{3+} ions in the vicinity of the growing sites could take place, facilitating the controlled formation of small gaps within the Au nanopillars. Figure 2 shows plan-view SEM images of Au nanostructures produced by RA treatment with varying reduction current density. When slow reduction rates (i.e., -2.0 mA cm^{-2}) were applied, the morphology of the Au structures appears to be pore-like structures, which are randomly connected with the adjacent structures. In contrast, vertically aligned and independently

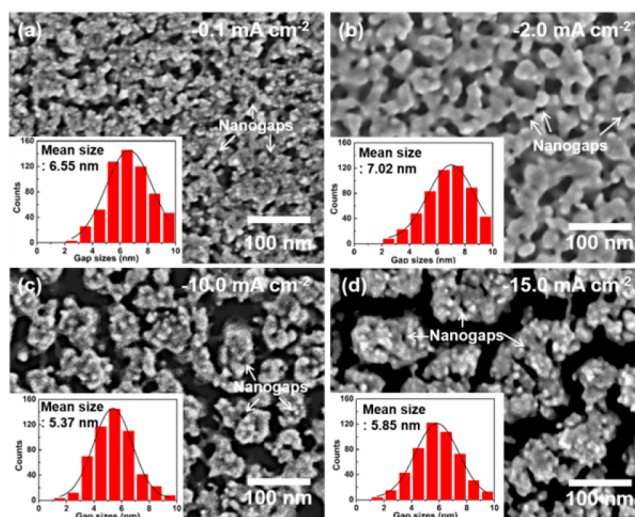


Figure 2. Plan-view SEM images of Au nanopillars produced by the RA treatment. Various reduction current density of (a) -0.1 mA cm^{-2} , (b) -2.0 mA cm^{-2} , (c) -10.0 mA cm^{-2} , and (d) -15.0 mA cm^{-2} , respectively. Insets show statistical histograms of the size distribution of nanogaps ($<10 \text{ nm}$) for the corresponding Au nanostructures.

standing Au nanopillars and nanoparticles (named unique 3D NPOP, as mentioned above) were obtained with high reduction rates (i.e., $\geq -10.0 \text{ mA cm}^{-2}$) (Figure 2 and Figure S1 in the Supporting Information).

Importantly, it is observed that the gap size distribution is changed with the applied reduction current density. As shown in the insets of Figure 2, the nanogap size distribution is statistically obtained by directly measuring the size and counting the number of sub-10 nm nanogaps from plan-view SEM images. It is found that the mean gap size of pillar-like Au nanostructures tends to be smaller than that of the randomly linked pore-like structures; for example, when the reduction current density is increased from -2.0 to -10.0 mA cm^{-2} , the mean gap size of the resulting Au nanostructure is diminished from 7.02 to 5.37 nm. It is noted that the gap of the Au pillars is indicative of the significantly narrow interstices ($<10 \text{ nm}$) within a single nanopillar instead of the relatively wide spacing (20–30 nm) between neighboring structures (as indicated by white arrows). In addition, the gap ($<10 \text{ nm}$) density per unit area of $1 \mu\text{m}^2$ is also prone to decrease with an increase of the reduction current density (Figure S2 in the Supporting Information). It should be noted that numerous nanoparticles protruded (or scattered) on Au nanostructures formed from the RA treatment (Figure 2 and Figure S1 in the Supporting Information). According to previous reports, the presence of metal nanoparticles distributed on the three-dimensional nanostructures can significantly increase the SERS intensity due to the increase of the areal density of hot spots.^{63,67} The number of nanoparticles protruded on the Au nanostructures per a unit volume gradually increases as the applied reduction current density is increased, as shown in Figure S3 in the Supporting Information. Although the number of wide nanogaps between pillars decreased with increasing reduction current density, the increased number of nanoparticles protruded during the reduction process and the resultant formation of many narrow nanogaps can effectively compensate for this factor.

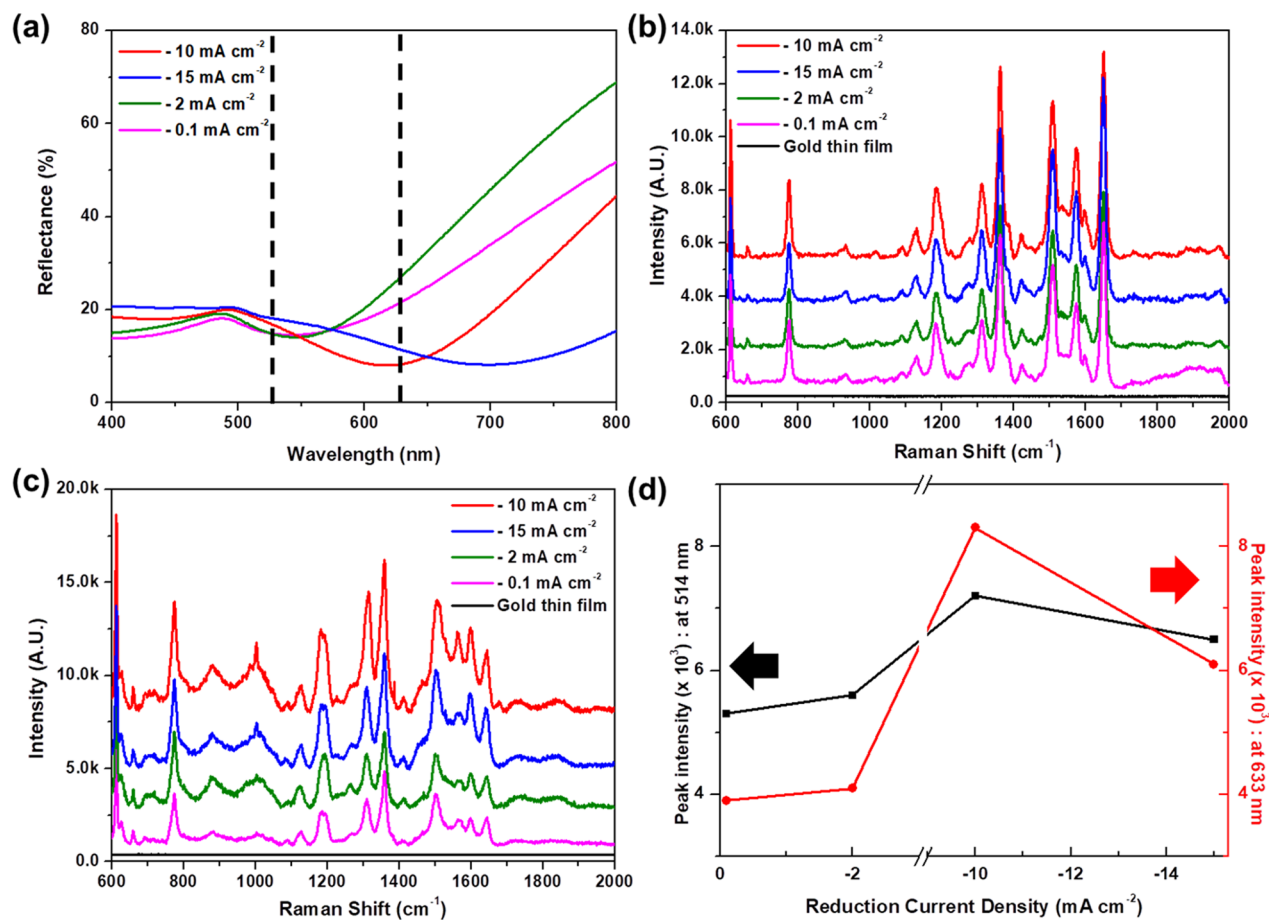


Figure 3. Reflectance spectra and SERS spectra of RA-treated Au samples. (a) Reflectance spectra of the nanoporous Au samples for various reduction current densities. (b–c) SERS spectra measured with different excitation laser wavelength: (b) 514 nm and (c) 633 nm. (d) Variation of SERS intensity (for the peak at 1363 cm⁻¹, the main characteristic peak of R6G) as a function of reduction current densities with different excitation laser wavelengths.

To analyze the optical properties of the Au nanostructures depending on the reduction conditions, the reflection spectra were obtained using UV–Visible spectroscopy. As shown in Figure 3a, the peaks of plasmonic resonance wavelength are clearly red-shifted with increasing reduction current density. To give a better understanding of the red-shifted reflectance spectra, simulated reflectance spectra using the finite element method (FEM) were obtained under the suggested simulation model, as shown in Figure S8. When the diameter (S) of the nanopillars is increased, the reflectance spectrum is significantly red-shifted, which is consistent with the experimental results in Figure 3a. The peak position shifted from 539 to 705 nm as the reduction current was increased from -0.1 to -15 mA cm⁻² (see also Figure S4 in the Supporting Information). The reflectance in the UV–Vis spectra for the different reduction currents was also compared at the wavelengths of 514 and 633 nm, which are the excitation wavelengths for SERS measurements. As shown by the dashed lines in Figure 3a, the reflectance difference at 514 nm was negligible, and therefore this would not affect the enhancement of the SERS signal. On the other hand, a significant difference in the reflectance value at the wavelength of 633 nm can intensify the SERS signal produced by the laser source with the same wavelength. To explore the SERS effect of the various RA-treated Au nanostructures using different laser excitation sources, a diluted Rhodamine 6G (R6G) solution with a

concentration of 10^{-6} M was used as the probe molecule. A high-resolution dispersive Raman microscope was used for SERS measurement. A 10^{-6} M solution ($7 \mu\text{L}$) of R6G was dropped on the SERS substrate with 514 and 633 nm excitation lasers and 7 s acquisition time. Figure 3b,c comparatively presents the SERS spectra of the Au nanostructures measured with 514 and 633 nm excitation sources, respectively. The characteristic peaks of R6G were clearly recognized at 775, 1190, 1363, and 1651 cm⁻¹. The intensities of characteristic SERS peaks significantly varied with the reduction conditions. This can be explained based on the absorption characteristics of the sample and nanogap sizes and densities.^{41,42,63} To quantify the dependency of the SERS intensity on the excitation wavelength and structural factor, the height of the SERS peaks at 1363 cm⁻¹, which is the main characteristic peak of R6G, was compared, as depicted in Figure 3d. Given that the differences in the reflectance value of the Au nanostructure are negligible at 514 nm, we can conclude that the peak height tendency for 514 nm excitation is highly related to the structural factor (nanogap size). As a result, the Au nanostructures fabricated with a -10 mA cm⁻² reduction current density (the sample with the smallest nanogap size) show superior SERS enhancement. On the other hand, the strong signal intensity obtained with the 3D NPOP structure (reduction current = -10 mA cm⁻²) and 633 nm laser excitation can be explained by the added contribution

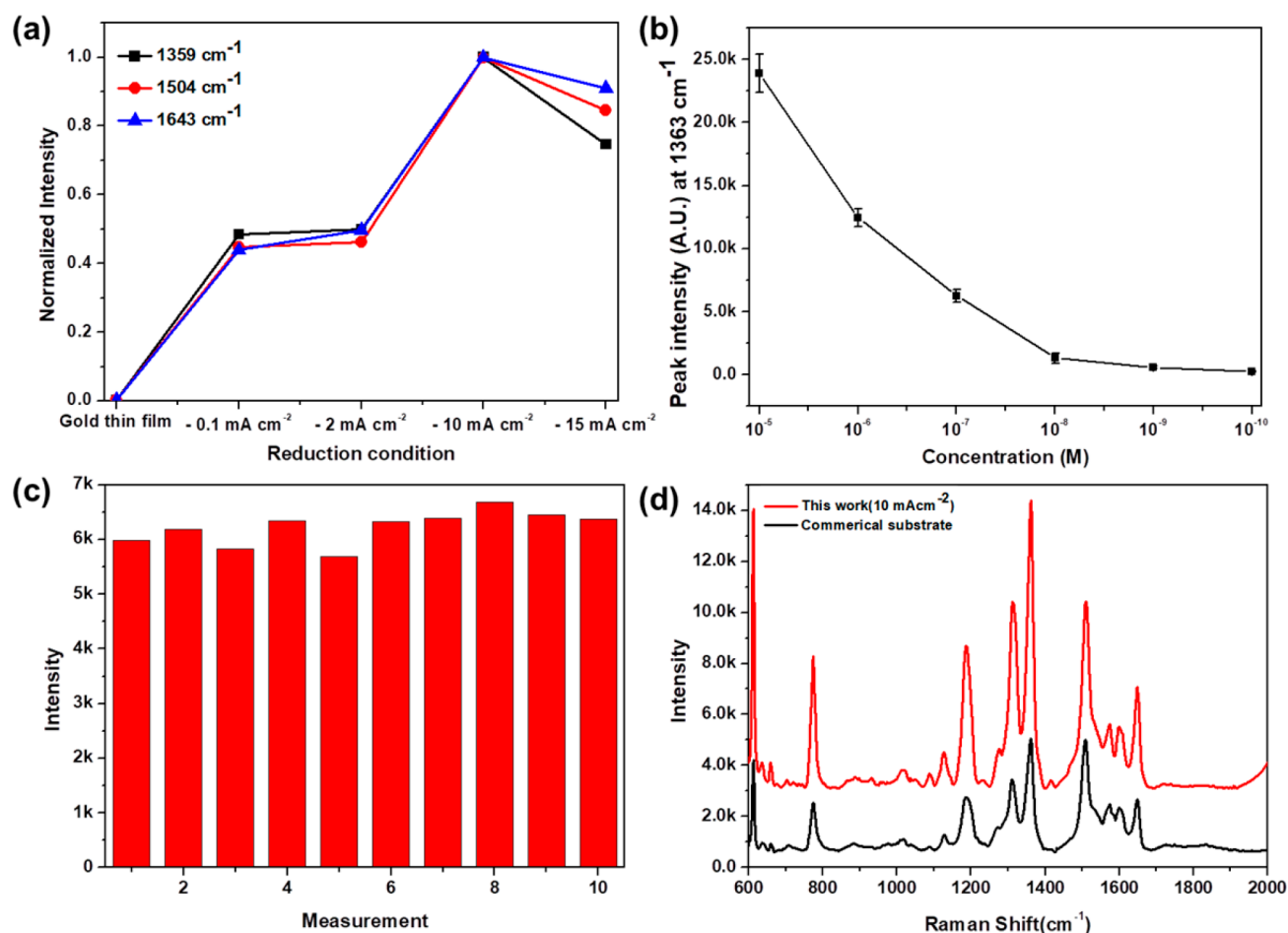


Figure 4. SERS analysis data of the 3D NPOP Au structures. (a) Normalized SERS intensities as a function of reduction current density. The intensity of the Au thin film is also shown for comparison. (b) 3D NPOP Au structure (reduction current = -10 mA cm^{-2}): SERS intensity change of R6G molecules for the main peak occurring at 1363 cm^{-1} depending on R6G concentration. (c) Distribution of SERS intensity collected from 10 randomly measured spots (reduction current = -10 mA cm^{-2}). (d) Comparison of the 3D NPOP Au SERS spectra with a commercial substrate (Silmecco substrate).

by the structural effect and also by the better matching of the plasmonic resonance wavelength with the measurement laser wavelength. In this sense, our nanostructured Au SERS substrate exhibits synergistic enhancement for maximizing the SERS enhancement effect at the 633 nm excitation laser wavelength. A more systematic evaluation of the SERS performance of the sample was also conducted. As shown in Figure 4a, the normalized SERS signal intensity clearly demonstrates the superior SERS effect for the 3D NPOP structure (for comparison, corresponding data for a Au thin film are also shown). As shown in Figure 4b, as the concentration of R6G molecules is diluted, the height of the peak occurring at 1363 cm^{-1} is gradually decreased (full SERS spectra are provided in Figure S5 in the Supporting Information). Characteristic peaks of R6G molecules were clearly distinguishable even at the nanomolar level. Figure 4c presents the SERS intensities measured from 10 random positions, and from these data, the standard deviation of intensity divided by the average intensity was calculated to be 9.7%. To evaluate the degree of SERS enhancement more quantitatively, the average enhancement factor (AEF) was also calculated with R6G molecules. The AEF can be calculated using the following equation:²³

$$\text{AEF} = \frac{I_{\text{SERS}} \times N_{\text{Film}}}{I_{\text{Film}} \times N_{\text{SERS}}}$$

where I_{SERS} and N_{SERS} represent the intensity and number of molecules on the SERS substrate, estimated by drop-casting $7 \mu\text{L}$ of 10^{-6} M R6G solution on the 3D NPOP SERS substrate, and I_{Film} and N_{Film} represent the intensity and number of molecules measured after dropping the same amount of R6G solution on a Si wafer. The calculated AEF value of the 3D NPOP structure was 7.2×10^5 , which is comparable with the highest values for nanostructured Au substrates for SERS enhancement.^{68–70} This enables trace level detection of the molecule. Moreover, the 3D NPOP SERS substrate fabricated in this study recorded approximately three-times higher signal height compared to a commercial SERS substrate (Figure 4d).

In order to demonstrate extended functionality of our Au nanostructures for SERS-based sensors, we attached aptamer probes to enable highly sensitive and selective detection of Hg^{2+} ions. The schematic procedure for the 3D-NPOP Au nanostructure based aptamer sensor is illustrated in Figure 5a. Aptamers are short single strand DNA oligonucleotides that can recognize specific target molecules by forming three-dimensional structures.⁷¹ Hg^{2+} ion-specific aptamers consisted of multiple thymine base molecules⁷² with an alkanethiol moiety (-SH) at the 5'-end and a cyanine (Cy5) tag at the 3'-

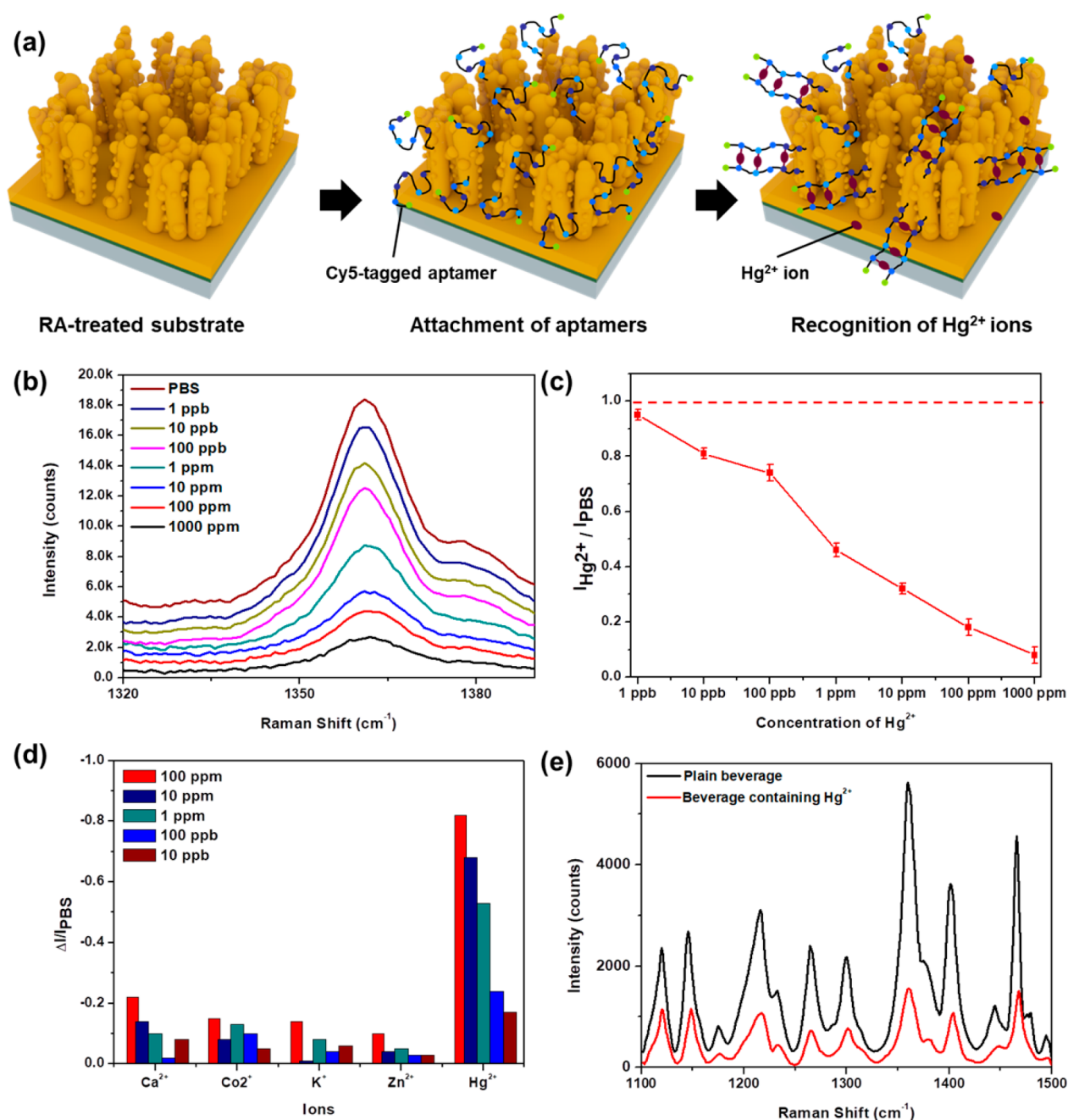


Figure 5. Fabrication and characterization of aptamer-functionalized SERS sensor. (a) Schematic procedure for the attachment of aptamer on the 3D NPOP SERS substrate. (b) Comparison of SERS peaks occurring at 1365 cm⁻¹ (originated from the strong vibration mode of Cy5) as a function of the concentration of Hg²⁺ in PBS buffer solution. (c) Normalized peak intensity (*I*) of the data shown in (b). The intensity of pure PBS buffer solution without containing Hg²⁺ is indicated by a dashed line for comparison. (d) Selective detection of Hg²⁺ ions using the aptamer-functionalized SERS sensor. The intensity is normalized with that for the PBS blank sample. (e) Selectivity test results applied to conventional beverage with and without Hg²⁺ ions.

end were anchored to our 3D-NPOP Au nanostructures based on a previously reported method.⁵⁸ Attachment of aptamers was achieved through Au-thiolate covalent bonding^{73–75} and successful immobilization was confirmed by characteristic SERS signals of Cy5 tags showing strong vibrational modes at 1365 cm⁻¹, as presented in Figure S6. The initially strong SERS enhancement of Cy5 tags can be attributed to the flexible aptamers lying on the Au surface in the absence of Hg²⁺ ions. In the presence of analytes, aptamers bind to Hg²⁺ ions by forming thymine-Hg²⁺-thymine pairs in rigid duplex-like structures,⁷⁷ placing the Cy5 tags further from the Au

surface, resulting in reduced SERS signals of Cy5 tags.^{58,76} Figure 5b,c shows a linear decrease of Cy5 tag SERS intensities with increasing concentration of Hg²⁺ ions down to the 10 ppb level, due to the increased fraction of duplex-like aptamer structures. In addition, we observed selective recognition of Hg²⁺ ions among other metal ions (Ca²⁺, Co²⁺, K⁺, Zn²⁺). In Figure 5d, the SERS intensity showed a significantly larger change for Hg²⁺ ions with increasing concentration, thus verifying prominent selectivity to Hg²⁺ ions. Further tests conducted in common drinking beverages mixed with metallic ions successfully confirmed selective detection in complex

media (Figure 5e and Figure S7 in the Supporting Information). Owing to such high sensitivity and selectivity, our aptamer-functionalized SERS sensors are not only suitable for trace-amount molecule detection, but also are expected to be used in more challenging sensing environments.

CONCLUSION

In this work, we presented a highly facile and scalable fabrication method for high-density Au nanopillar arrays containing narrow nanogaps, targeting applications for high-performance SERS substrates. By a sequential oxidation and reduction process, nanostructured gold with high-density nanogaps (especially 3D nanopillars decorated with nanoparticles) were controllably produced. As the reduction current increased, the plasmonic resonance wavelengths of the samples were clearly red-shifted, enabling successful tuning of optical characteristics of the SERS substrate to match its resonance wavelength with the excitation wavelength (633 nm) of the incident laser beam. Optimization of the structural factor of the gold nanostructure and matching the plasmonic resonance wavelength provide synergistic enhancement of the SERS signal. These strategies enabled a high average enhancement factor over 10^5 and highly reproducible SERS signal intensity (standard deviation of 9.7%), and successful detection of trace molecules (\sim nM) with high uniformity was demonstrated. Moreover, an aptamer-functionalized SERS substrate demonstrated outstanding detection sensitivity of \sim 10 ppb for Hg ions. This facile, low-cost, scalable fabrication strategy can be a practical candidate for various sensing and detection platforms based on well-controlled nanoplasmonic structures.

ASSOCIATED CONTENT

Supporting Information

The Supporting Information is available free of charge on the ACS Publications website at DOI: 10.1021/acs.chemmater.8b02995.

Related experimental data (PDF)

AUTHOR INFORMATION

Corresponding Authors

*Y. S. Jung. E-mail: ysjung@kaist.ac.kr.

*J. Oh. E-mail: jihun.oh@kaist.ac.kr.

ORCID

Jaehoon Kim: 0000-0002-3080-8743

Min Seok Jang: 0000-0002-5683-1925

Jihun Oh: 0000-0001-6465-6736

Yeon Sik Jung: 0000-0002-7709-8347

Author Contributions

[†]K.M.B. and J.K. contributed equally to this work.

Notes

The authors declare no competing financial interest.

ACKNOWLEDGMENTS

This work was supported by the Center for Integrated Smart Sensors funded by the Ministry of Science and ICT as Global Frontier Project[†] (CISS-2011-0031848). This research was also supported by the Korea CCS R&D Center (Korea CCS 2020 Project) grant funded by the Korea government (Ministry of Science and ICT), Grant No. NRF-2014M1A8A1049303. S. K. and M. S. J. acknowledge support from Creative Materials Discovery Program through the

National Research Foundation of Korea funded by Ministry of Science and ICT (2016M3D1A1900038).

REFERENCES

- (1) Nriagu, J. O.; Pacyna, J. M. Quantitative Assessment of Worldwide Contamination of Air, Water and Soils by Trace-Metals. *Nature* **1988**, *333*, 134–139.
- (2) Albrecht, M. G.; Creighton, J. A. Anomalous Intense Raman Spectra of Pyridine at a Silver Electrode. *J. Am. Chem. Soc.* **1977**, *99*, 5215–5217.
- (3) Stiles, P. L.; Dieringer, J. A.; Shah, N. C.; Van Duyne, R. R. Surface-Enhanced Raman Spectroscopy. *Annu. Rev. Anal. Chem.* **2008**, *1*, 601–626.
- (4) Fleischmann, M.; Hendra, P. J.; McQuillan, A. J. Raman-Spectra of Pyridine Adsorbed at a Silver Electrode. *Chem. Phys. Lett.* **1974**, *26*, 163–166.
- (5) Willets, K. A.; Van Duyne, R. P. Localized surface plasmon resonance spectroscopy and sensing. *Annu. Rev. Phys. Chem.* **2007**, *58*, 267–297.
- (6) Yang, W. H.; Hulteen, J.; Schatz, G. C.; VanDuyne, R. P. A surface-enhanced hyper-Raman and surface-enhanced Raman scattering study of trans-1,2-bis(4-pyridyl)ethylene adsorbed onto silver film over nanosphere electrodes. Vibrational assignments: Experiment and theory. *J. Chem. Phys.* **1996**, *104*, 4313–4323.
- (7) Moskovits, M. Surface-Enhanced Spectroscopy. *Rev. Mod. Phys.* **1985**, *57*, 783–826.
- (8) Tao, A.; Kim, F.; Hess, C.; Goldberger, J.; He, R. R.; Sun, Y. G.; Xia, Y. N.; Yang, P. D. Langmuir-Blodgett silver nanowire monolayers for molecular sensing using surface-enhanced Raman spectroscopy. *Nano Lett.* **2003**, *3*, 1229–1233.
- (9) Le, F.; Brandl, D. W.; Urzhumov, Y. A.; Wang, H.; Kundu, J.; Halas, N. J.; Aizpurua, J.; Nordlander, P. Metallic nanoparticle arrays: A common substrate for both surface-enhanced Raman scattering and surface-enhanced infrared absorption. *ACS Nano* **2008**, *2*, 707–718.
- (10) GarciaVidal, F. J.; Pendry, J. B. Collective theory for surface enhanced Raman scattering. *Phys. Rev. Lett.* **1996**, *77*, 1163–1166.
- (11) Craig, A. P.; Franca, A. S.; Irudayaraj, J. Surface-Enhanced Raman Spectroscopy Applied to Food Safety. *Annu. Rev. Food Sci. Technol.* **2013**, *4*, 369–380.
- (12) Sharma, B.; Frontiera, R. R.; Henry, A. I.; Ringe, E.; Van Duyne, R. P. SERS: Materials, applications, and the future. *Mater. Today* **2012**, *15*, 16–25.
- (13) Shih, W.-C.; Santos, G. M.; Zhao, F.; Zenasni, O.; Arnob, M. M. P. Simultaneous Chemical and Refractive Index Sensing in the 1–2.5 μ m Near-Infrared Wavelength Range on Nanoporous Gold Disks. *Nano Lett.* **2016**, *16*, 4641–4647.
- (14) Nikoobakht, B.; El-Sayed, M. A. Surface-enhanced Raman scattering studies on aggregated gold nanorods. *J. Phys. Chem. A* **2003**, *107*, 3372–3378.
- (15) Kang, J. W.; So, P. T. C.; Dasari, R. R.; Lim, D. K. High Resolution Live Cell Raman Imaging Using Subcellular Organelle-Targeting SERS-Sensitive Gold Nanoparticles with Highly Narrow Intra-Nanogap. *Nano Lett.* **2015**, *15*, 1766–1772.
- (16) Duan, H. G.; Hu, H. L.; Hui, H. K.; Shen, Z. X.; Yang, J. K. W. Free-standing sub-10 nm nanostencils for the definition of gaps in plasmonic antennas. *Nanotechnology* **2013**, *24*, 185301.
- (17) Gunnarsson, L.; Bjerneld, E. J.; Xu, H.; Petronis, S.; Kasemo, B.; Kall, M. Interparticle coupling effects in nanofabricated substrates for surface-enhanced Raman scattering. *Appl. Phys. Lett.* **2001**, *78*, 802–804.
- (18) Wang, H.; Levin, C. S.; Halas, N. J. Nanosphere arrays with controlled sub-10-nm gaps as surface-enhanced Raman spectroscopy substrates. *J. Am. Chem. Soc.* **2005**, *127*, 14992–14993.
- (19) Ward, D. R.; Grady, N. K.; Levin, C. S.; Halas, N. J.; Wu, Y. P.; Nordlander, P.; Natelson, D. Electromigrated nanoscale gaps for surface-enhanced Raman spectroscopy. *Nano Lett.* **2007**, *7*, 1396–1400.

- (20) Chen, X. S.; Ciraci, C.; Smith, D. R.; Oh, S. H. Nanogap-Enhanced Infrared Spectroscopy with Template-Stripped Wafer-Scale Arrays of Buried Plasmonic Cavities. *Nano Lett.* **2015**, *15*, 107–113.
- (21) Duan, H. G.; Hu, H. L.; Kumar, K.; Shen, Z. X.; Yang, J. K. W. Direct and Reliable Patterning of Plasmonic Nanostructures with Sub-10-nm Gaps. *ACS Nano* **2011**, *5*, 7593–7600.
- (22) Ding, T.; Herrmann, L. O.; de Nijs, B.; Benz, F.; Baumberg, J. J. Self-Aligned Colloidal Lithography for Controllable and Tuneable Plasmonic Nanogaps. *Small* **2015**, *11*, 2139–2143.
- (23) Jeong, J. W.; Arnob, M. M. P.; Baek, K. M.; Lee, S. Y.; Shih, W. C.; Jung, Y. S. 3D Cross-Point Plasmonic Nanoarchitectures Containing Dense and Regular Hot Spots for Surface-Enhanced Raman Spectroscopy Analysis. *Adv. Mater.* **2016**, *28*, 8695–8704.
- (24) Baek, K. M.; Kim, J. M.; Jeong, J. W.; Lee, S. Y.; Jung, Y. S. Sequentially Self-Assembled Rings-in-Mesh Nanoplasmonic Arrays for Surface-Enhanced Raman Spectroscopy. *Chem. Mater.* **2015**, *27*, 5007–5013.
- (25) Fulmes, J.; Jäger, R.; Bräuer, A.; Schäfer, C.; Jäger, S.; Gollmer, D. A.; Horrer, A.; Nadler, E.; Chassé, T.; Zhang, D.; Meixner, A. J.; Kern, D. P.; Fleischer, M. Self-aligned placement and detection of quantum dots on the tips of individual conical plasmonic nanostructures. *Nanoscale* **2015**, *7*, 14691–14696.
- (26) Horrer, A.; Schäfer, C.; Broch, K.; Gollmer, D. A.; Rogalski, J.; Fulmes, J.; Zhang, D.; Meixner, A. J.; Schreiber, F.; Kern, D. P.; Fleischer, M. Parallel Fabrication of Plasmonic Nanocone Sensing Arrays. *Small* **2013**, *9*, 3987–3992.
- (27) Lin, D.; Wu, Z.; Li, S.; Zhao, W.; Ma, C.; Wang, J.; Jiang, Z.; Zhong, Z.; Zheng, Y.; Yang, X. Large-Area Au-Nanoparticle-Functionalized Si Nanorod Arrays for Spatially Uniform Surface-Enhanced Raman Spectroscopy. *ACS Nano* **2017**, *11*, 1478–1487.
- (28) Lee, B.-S.; Lin, D.-Z.; Yen, T.-J. A Low-cost, Highly-stable Surface Enhanced Raman Scattering Substrate by Si Nanowire Arrays Decorated with Au Nanoparticles and Au Backplate. *Sci. Rep.* **2017**, *7*, 4604.
- (29) Ahn, H.-J.; Thiyagarajan, P.; Jia, L.; Kim, S.-I.; Yoon, J.-C.; Thomas, E. L.; Jang, J.-H. An optimal substrate design for SERS: dual-scale diamond-shaped gold nano-structures fabricated via interference lithography. *Nanoscale* **2013**, *5*, 1836.
- (30) Lim, D.-K.; Jeon, K.-S.; Hwang, J.-H.; Kim, H.; Kwon, S.; Suh, Y. D.; Nam, J.-M. Highly uniform and reproducible surface-enhanced Raman scattering from DNA-tailorable nanoparticles with 1-nm interior gap. *Nat. Nanotechnol.* **2011**, *6*, 452–460.
- (31) Osberg, K. D.; Rycenga, M.; Harris, N.; Schmucker, A. L.; Langille, M. R.; Schatz, G. C.; Mirkin, C. A. Dispersible gold nanorod dimers with sub-5 nm gaps as local amplifiers for surface-enhanced Raman scattering. *Nano Lett.* **2012**, *12*, 3828–3832.
- (32) Si, S.; Liang, W.; Sun, Y.; Huang, J.; Ma, W.; Liang, Z.; Bao, Q.; Jiang, L. Facile Fabrication of High-Density Sub-1-nm Gaps from Au Nanoparticle Monolayers as Reproducible SERS Substrates. *Adv. Funct. Mater.* **2016**, *26*, 8137–8145.
- (33) Im, H.; Bantz, K. C.; Lindquist, N. C.; Haynes, C. L.; Oh, S.-H. Vertically Oriented Sub-10-nm Plasmonic Nanogap Arrays. *Nano Lett.* **2010**, *10*, 2231–2236.
- (34) Zeng, J.; Zhao, F.; Li, M.; Li, C.-H.; Lee, T. R.; Shih, W.-C. Morphological control and plasmonic tuning of nanoporous gold disks by surface modifications. *J. Mater. Chem. C* **2015**, *3*, 247–252.
- (35) Chen, X.; Lindquist, N. C.; Klemme, D. J.; Nagpal, P.; Norris, D. J.; Oh, S.-H. Split-Wedge Antennas with Sub-5 nm Gaps for Plasmonic Nanofocusing. *Nano Lett.* **2016**, *16*, 7849–7856.
- (36) Im, H.; Bantz, K. C.; Lee, S. H.; Johnson, T. W.; Haynes, C. L.; Oh, S.-H. Self-Assembled Plasmonic Nanoring Cavity Arrays for SERS and LSPR Biosensing. *Adv. Mater.* **2013**, *25*, 2678–2685.
- (37) Chen, X.; Park, H.-R.; Pelton, M.; Piao, X.; Lindquist, N. C.; Im, H.; Kim, Y. J.; Ahn, J. S.; Ahn, K. J.; Park, N.; Kim, D.-S.; Oh, S.-H. Atomic layer lithography of wafer-scale nanogap arrays for extreme confinement of electromagnetic waves. *Nat. Commun.* **2013**, *4*, 2361.
- (38) Kanipe, K. N.; Chidester, P. P. F.; Stucky, G. D.; Moskovits, M. Large Format Surface-Enhanced Raman Spectroscopy Substrate Optimized for Enhancement and Uniformity. *ACS Nano* **2016**, *10*, 7566–7571.
- (39) Ma, C.; Gao, Q.; Hong, W.; Fan, J.; Fang, J. Real-Time Probing Nanopore-in-Nanogap Plasmonic Coupling Effect on Silver Super-crystals with Surface-Enhanced Raman Spectroscopy. *Adv. Funct. Mater.* **2017**, *27*, 1603233.
- (40) Li, X.-M.; Bi, M.-H.; Cui, L.; Zhou, Y.-Z.; Du, X.-W.; Qiao, S.-Z.; Yang, J. 3D Aluminum Hybrid Plasmonic Nanostructures with Large Areas of Dense Hot Spots and Long-Term Stability. *Adv. Funct. Mater.* **2017**, *27*, 1605703.
- (41) Lee, W.; Lee, S. Y.; Briber, R. M.; Rabin, O. Self-Assembled SERS Substrates with Tunable Surface Plasmon Resonances. *Adv. Funct. Mater.* **2011**, *21*, 3424–3429.
- (42) Kang, M.; Kim, J.-J.; Oh, Y.-J.; Park, S.-G.; Jeong, K.-H. Nanoplasmonics: A Deformable Nanoplasmonic Membrane Reveals Universal Correlations Between Plasmon Resonance and Surface Enhanced Raman Scattering. *Adv. Mater.* **2014**, *26*, 4509–4509.
- (43) Lin, X.-M.; Cui, Y.; Xu, Y.-H.; Ren, B.; Tian, Z.-Q. Surface-enhanced Raman spectroscopy: substrate-related issues. *Anal. Bioanal. Chem.* **2009**, *394*, 1729–1745.
- (44) Zhu, Z.; Meng, H.; Liu, W.; Liu, X.; Gong, J.; Qiu, X.; Jiang, L.; Wang, D.; Tang, Z. Superstructures and SERS Properties of Gold Nanocrystals with Different Shapes. *Angew. Chem.* **2011**, *123*, 1631–1634.
- (45) Tang, B.; Wang, J.; Hutchison, J. A.; Ma, L.; Zhang, N.; Guo, H.; Hu, Z.; Li, M.; Zhao, Y. Ultrasensitive, Multiplex Raman Frequency Shift Immunoassay of Liver Cancer Biomarkers in Physiological Media. *ACS Nano* **2016**, *10*, 871–879.
- (46) Hu, Y.; Cheng, H.; Zhao, X.; Wu, J.; Muhammad, F.; Lin, S.; He, J.; Zhou, L.; Zhang, C.; Deng, Y.; Wang, P.; Zhou, Z.; Nie, S.; Wei, H. Surface-Enhanced Raman Scattering Active Gold Nanoparticles with Enzyme-Mimicking Activities for Measuring Glucose and Lactate in Living Tissues. *ACS Nano* **2017**, *11*, 5558–5566.
- (47) Huang, Z.; Meng, G.; Huang, Q.; Yang, Y.; Zhu, C.; Tang, C. Improved SERS Performance from Au Nanopillar Arrays by Abridging the Pillar Tip Spacing by Ag Sputtering. *Adv. Mater.* **2010**, *22*, 4136–4139.
- (48) Abdelsalam, M. E.; Mahajan, S.; Bartlett, P. N.; Baumberg, J. J.; Russell, A. E. SERS at Structured Palladium and Platinum Surfaces. *J. Am. Chem. Soc.* **2007**, *129*, 7399–7406.
- (49) Habouti, S.; Mátéfi-Tempfli, M.; Solterbeck, C.-H.; Es-Souni, M.; Mátéfi-Tempfli, S.; Es-Souni, M. On-substrate, self-standing Au-nanorod arrays showing morphology controlled properties. *Nano Today* **2011**, *6*, 12–19.
- (50) Bae, D. R.; Chang, S.-J.; Huh, Y. S.; Han, Y.-K.; Lee, Y.-J.; Yi, G.-R.; Kim, S.; Lee, G. Surfactant Size Effect on Surface-Enhanced Raman Scattering Intensity from Silver Nanoparticles. *J. Nanosci. Nanotechnol.* **2013**, *13*, 5840–5843.
- (51) Chen, Y.; Li, C. W.; Kanan, M. W. Aqueous CO₂ Reduction at Very Low Overpotential on Oxide-Derived Au Nanoparticles. *J. Am. Chem. Soc.* **2012**, *134*, 19969–19972.
- (52) Ma, M.; Trześniewski, B. J.; Xie, J.; Smith, W. A. Selective and Efficient Reduction of Carbon Dioxide to Carbon Monoxide on Oxide-Derived Nanostructured Silver Electrocatalysts. *Angew. Chem.* **2016**, *128*, 9900–9904.
- (53) Song, J. T.; Ryoo, H.; Cho, M.; Kim, J.; Kim, J.-G.; Chung, S.-Y.; Oh, J. Nanoporous Au Thin Films on Si Photoelectrodes for Selective and Efficient Photoelectrochemical CO₂ Reduction. *Adv. Energy Mater.* **2017**, *7*, 1601103.
- (54) Kim, J.; Song, J. T.; Ryoo, H.; Kim, J.-G.; Chung, S.-Y.; Oh, J. Morphology-controlled Au nanostructures for efficient and selective electrochemical CO₂ reduction. *J. Mater. Chem. A* **2018**, *6*, 5119–5128.
- (55) Vela, M. E.; Salvarezza, R. C.; Arvia, A. J. The electroreduction kinetics of the hydrous gold oxide layers and growth modes and roughness of the electroreduced gold overlayers. *Electrochim. Acta* **1990**, *35*, 117–125.

- (56) Wan, Y.; Wang, X. L.; Liu, S. Y.; Li, Y. B.; Sun, H.; Wang, Q. Effect of Electrochemical Factors on Formation and Reduction of Silver Oxides. *Int. J. Electrochem. Soc.* **2013**, *8*, 12837–12850.
- (57) Jee, M. S.; Jeon, H. S.; Kim, C.; Lee, H.; Koh, J. H.; Cho, J.; Min, B. K.; Hwang, Y. J. Enhancement in carbon dioxide activity and stability on nanostructured silver electrode and the role of oxygen. *Appl. Catal., B* **2016**, *180*, 372–378.
- (58) Zhang, L.; Chang, H.; Hirata, A.; Wu, H.; Xue, Q.-K.; Chen, M. Nanoporous Gold Based Optical Sensor for Sub-ppt Detection of Mercury Ions. *ACS Nano* **2013**, *7*, 4595–4600.
- (59) Johnson, P. B.; Christy, R. W. Optical Constants of the Noble Metals. *Phys. Rev. B* **1972**, *6*, 4370–4379.
- (60) Palik, E. D. *Handbook of Optical Constants of Solids*; Elsevier: New York, 1997.
- (61) Tremiliosi-Filho, G.; Dall'Antonia, L. H.; Jerkiewicz, G. Limit to extent of formation of the quasi-two-dimensional oxide state on Au electrodes. *J. Electroanal. Chem.* **1997**, *422*, 149–159.
- (62) Juodkakis, K. XPS studies on the gold oxide surface layer formation. *Electrochem. Commun.* **2000**, *2*, 503–507.
- (63) Oh, Y.-J.; Jeong, K.-H. Glass Nanopillar Arrays with Nanogap-Rich Silver Nanoislands for Highly Intense Surface Enhanced Raman Scattering. *Adv. Mater.* **2012**, *24*, 2234–2237.
- (64) Albano, E. V. Monte Carlo Simulation of a Model for Growth Kinetics and Growth Mode of Metals Through Hydrous Metal Oxide Layers Electroreduction. Applications to Gold Overlayers. *J. Electrochem. Soc.* **1990**, *137*, 117.
- (65) Liu, M.; Pang, Y.; Zhang, B.; De Luna, P.; Voznyy, O.; Xu, J.; Zheng, X.; Dinh, C. T.; Fan, F.; Cao, C.; de Arquer, F. P. G.; Safaei, T. S.; Mepham, A.; Klinkova, A.; Kumacheva, E.; Filleter, T.; Sinton, D.; Kelley, S. O.; Sargent, E. H. Enhanced electrocatalytic CO₂ reduction via field-induced reagent concentration. *Nature* **2016**, *537*, 382–386.
- (66) Saberi Safaei, T.; Mepham, A.; Zheng, X.; Pang, Y.; Dinh, C.-T.; Liu, M.; Sinton, D.; Kelley, S. O.; Sargent, E. H. High-Density Nanosharp Microstructures Enable Efficient CO₂ Electroreduction. *Nano Lett.* **2016**, *16*, 7224–7228.
- (67) Choi, S.; Ahn, M.; Kim, J. Highly reproducible surface-enhanced Raman scattering-active Au nanostructures prepared by simple electrodeposition: Origin of surface-enhanced Raman scattering activity and applications as electrochemical substrates. *Anal. Chim. Acta* **2013**, *779*, 1–7.
- (68) Rodrigues, D. C.; Andrade, G. F. S.; Temperini, M. L. A. SERS performance of gold nanotubes obtained by sputtering onto polycarbonate track-etched membranes. *Phys. Chem. Chem. Phys.* **2013**, *15*, 1169–1176.
- (69) Le Ru, E. C.; Blackie, E.; Meyer, M.; Etchegoin, P. G. Surface Enhanced Raman Scattering Enhancement Factors: A Comprehensive Study. *J. Phys. Chem. C* **2007**, *111*, 13794–13803.
- (70) Scarabelli, L.; Coronado-Puchau, M.; Giner-Casares, J. J.; Langer, J.; Liz-Marzán, L. M. Monodisperse Gold Nanotriangles: Size Control, Large-Scale Self-Assembly, and Performance in Surface-Enhanced Raman Scattering. *ACS Nano* **2014**, *8*, 5833–5842.
- (71) Liu, J.; Cao, Z.; Lu, Y. Functional Nucleic Acid Sensors. *Chem. Rev.* **2009**, *109*, 1948–1998.
- (72) Tanaka, Y.; Oda, S.; Yamaguchi, H.; Kondo, Y.; Kojima, C.; Ono, A. ¹⁵N–¹⁵N J-coupling across HgII: direct observation of HgII-mediated T–T base pairs in a DNA duplex. *J. Am. Chem. Soc.* **2007**, *129*, 244–245.
- (73) Herne, T. M.; Tarlov, M. J. Characterization of DNA Probes Immobilized on Gold Surfaces. *J. Am. Chem. Soc.* **1997**, *119*, 8916–8920.
- (74) Ron, H.; Rubinstein, I. Alkanethiol Monolayers on Preoxidized Gold. Encapsulation of Gold Oxide under an Organic Monolayer. *Langmuir* **1994**, *10*, 4566–4573.
- (75) Xu, L.; Zhao, S.; Ma, W.; Wu, X.; Li, S.; Kuang, H.; Wang, L.; Xu, C. Multigaps Embedded Nanoassemblies Enhance In Situ Raman Spectroscopy for Intracellular Telomerase Activity Sensing. *Adv. Funct. Mater.* **2016**, *26*, 1602–1608.
- (76) Miyake, Y.; Togashi, H.; Tashiro, M.; Yamaguchi, H.; Oda, S.; Kudo, M.; Tanaka, Y.; Kondo, Y.; Sawa, R.; Fujimoto, T.; Machinami, T.; Ono, A. MercuryII-Mediated Formation of Thymine–HgII–Thymine Base Pairs in DNA Duplexes. *J. Am. Chem. Soc.* **2006**, *128*, 2172–2173.
- (77) Liu, S.-J.; Nie, H.-G.; Jiang, J.-H.; Shen, G.-L.; Yu, R.-Q. Electrochemical Sensor for Mercury(II) Based on Conformational Switch Mediated by Interstrand Cooperative Coordination. *Anal. Chem.* **2009**, *81*, 5724–5730.